SLAC-PUB-16446

X-ray scattering measurements of dissociation-induced metallization of dynamically compressed deuterium

Authors: P. Davis[1,2*], T. Döppner[2], J.R. Rygg[2], C. Fortmann[2,3], L. Divol[2], A. Pak[2], L. Fletcher[4], A. Becker[5], B. Holst[5], P. Sperling[5], R. Redmer[5], M.P. Desjarlais[6], P. Celliers[2], G.W. Collins[2], O.L. Landen[2], R.W. Falcone[1], S.H. Glenzer[4]

Affiliations:
[1]University of California, Berkeley, Berkeley, CA 94709, USA

[2]Lawrence Livermore National Laboratory, PO Box 808, Livermore, CA 94551, USA

[3]University of California, Los Angeles, Los Angeles, CA 90095, USA

[4]SLAC National Accelerator Laboratory, Menlo Park, CA 94025, USA

[5]Institut für Physik, Universität Rostock, D-18051 Rostock, Germany

[6]Sandia National Laboratories, Albuquerque, NM 87185, USA

*Correspondence to: pfdavis@berkeley.edu

This material is based upon work supported by the U.S. Department of Energy, Office of Science, Office of Basic Energy Sciences, under Contract No. DE-AC02-76SF00515 and FES.

Abstract

Hydrogen, the simplest element in the universe, has a surprisingly complex phase diagram. Because of applications to planetary science, inertial confinement fusion and fundamental physics, its high-pressure properties have been the subject of intense study over the past two decades. While sophisticated static experiments have probed hydrogen's structure at ever higher pressures, studies examining the higher-temperature regime using dynamic compression have mostly been limited to optical measurement techniques. Here, we present the first spectrally resolved x-ray scattering measurements from plasmons in dynamically compressed deuterium. Combined with Compton scattering, and velocity interferometry to determine shock pressure and mass density, this allows us to extract ionization state as a function of compression. The onset of ionization occurs close in pressure to where density functional theory molecular dynamics (DFT-MD) simulations show molecular dissociation, suggesting hydrogen transitions from a molecular and insulating fluid to a conducting state without passing through an intermediate atomic phase.

Introduction

The insulator-metal transition in hydrogen has been a central problem in physics since Wigner and Huntington's 1935 prediction of a transformation of insulating molecular hydrogen to a monatomic conducting state at high pressure[1]. In recent decades, owing to fundamental questions about the structure of gas giants[2-6], hydrogen's high-pressure properties have been the subject of intense study. Diamond anvil cell experiments have explored the low-temperature, high-pressure structure of hydrogen. It has been shown to remain in an insulating, molecular state at pressures in excess of 300 GPa[7] and recent work has focused on its phases near room temperature[8-13]. Sophisticated *ab initio* simulation techniques have advanced in tandem, resulting in a wide computational exploration of the hydrogen phase diagram, see McMahon and coauthors[14].

High-pressures produced by dynamic compression techniques generally result in higher temperature conditions. Experiments by Nellis and coworkers used reverberating shock waves to produce conductive liquid hydrogen at 140 GPa and temperatures near 3000 K[15,16], reaching densities very close to those predicted by Wigner and Huntington[17]. Recent experiments using the Sandia Z machine reached 300 GPa and 1800 K, finding evidence for a liquid-liquid insulator-metal transition from optical reflectivity measurements[18]. In single-shock experiments, the temperatures reached are still higher, and the transition to metallic behavior is driven by the combined pressure and temperature reached in the shock front. These experiments produce thermodynamic states lying on the primary shock Hugoniot. Optical reflectivity measurements have been used to observe a transition to metallic behavior in laser-driven samples near 50 GPa and 8000 K[19]. X-ray scattering makes it possible to directly observe electron properties in such an experimental configuration, but until now it has not progressed beyond proof-of-principle in shock-compressed cryogenic samples[20]. In this work, we use a single-shock laser compression scheme, employing x-ray scattering to directly measure the ionization of laser-shocked deuterium as a function of compression.

Dynamic experiments along the principal Hugoniot result in target conditions far from the region where a first-order liquid-liquid phase transition from molecular to conducting fluids has been predicted[21, 22]. We illustrate this in the hydrogen phase diagram shown in Figure 1, which shows that most parts of the interiors of brown dwarfs (Gliese-229b, shown in brown) and giant planets (Jupiter, shown in black) are also at off-Hugoniot states. However, the P - T range of our experiments covers one of the most interesting parts of the Jovian interior. The flattening of the isentrope at about 25 GPa is due to the dissociation of the hydrogen molecules. As shown by French and coauthors[23], this is accompanied by a drastic increase in the dc electrical conductivity which represents a continuous nonmetal-to-metal transition. This result is validated with the x-ray scattering measurements presented in this study, where we find that the average ionization becomes significant just at this point on the Hugoniot curve, and coincident with dissociation. This is of great importance for planetary physics when validating EOS data that are used for interior[2,23] and dynamo models[24].

Inelastic x-ray scattering has a long history as a powerful probe of material properties in static samples. Recently, x-ray scattering has been employed in high-energy density physics experiments[28] using laser-produced x-ray sources to measure density and temperature in targets dynamically shocked to warm, dense conditions[29-32]. Experiments at the Omega laser have demonstrated the viability of backscattering techniques for density measurements in cryogenic deuterium[20]. Here, we combine forward and backward x-ray scattering observations with a simultaneous measurement of shock velocity using the VISAR technique to infer pressure and mass density from the velocity of the shock and equation of state (EOS) tables. With a delocalized electron density measured using x-ray scattering, we can then directly determine the ionization state of shocked deuterium as a function of compression. We compare the onset of ionization with the molecular dissociation fraction calculated from density functional theory molecular dynamics (DFT-MD) simulations and find that both quantities increase sharply between compressions of $2.5 \leq \rho/\rho_0 \leq 3.3$.

Results

X-ray scattering is sensitive to both the electron and ion structure in the target. The scattering cross section depends on the total dynamic structure factor of the material that, in the case of dense plasma conditions, is often expressed using a chemical picture approach due to Chihara[33,34] as $S_{ee}(k,\omega) = \left|f_I(k) + q(k)\right|^2 S_{ii}(k,\omega) + Z_f S_{ee}^0(k,\omega) + Z_b \int d\omega' \tilde{S}_{ce}(k,\omega-\omega') S_S(k,\omega')$. Here k is the wave-vector probed, $f(k)$ is the ionic form factor, $q(k)$ represents the electron screening cloud around the ion, and Z_f (Z_b) is the number of free (bound) electrons per atom. S_{ii} and S_{ee} represent the dynamic structure contributions of ions and free electrons; transitions of bound electrons into the continuum, S_{ce}, are modulated by the motion of the ions, represented by S_S.

In the non-relativistic limit, the probe energy and experimental geometry define the k-vectors probed according to $k = |\mathbf{k}| = 4\pi \frac{E_0}{hc} \sin(\theta/2)$. Our experiments probe density fluctuations at scale lengths of k=7.78×10^9 m^{-1} in the forward direction and 1.88×10^{10} m^{-1} in the backward direction. The scattering process can be defined with the parameter $\alpha=1/k\lambda_S$, where λ_S represents the screening length in the plasma. For the strongly degenerate systems studied in this work, the screening length can be approximated with the Thomas-Fermi length, and $\alpha=1/k\lambda_s=1/k\lambda_{TF}=$ $\frac{1}{k}\sqrt{\frac{4m_e e^2}{\hbar^2}\left(\frac{3n_e}{\pi}\right)^{1/3}}$, where n_e is the free electron density. Thus, for our conditions, the forward scattering vector extends beyond the screening length and provides collective scattering even at small ionization fractions[35], while the backward scattering vector is sufficiently long to probe at a scale length smaller than the screening length of the plasma, observing the electron momentum distribution in the Compton limit[36].

A series of cryogenic experiments was performed at the Janus Laser Facility at the Lawrence Livermore National Laboratory, a schematic of which is shown in Figure 2. A drive laser was focused onto a cryogenic target, launching a shock wave into liquid deuterium at an initial density ρ_0=0.17±0.004 g cm^{-3}. A second laser, incident on a Si_3N_4 foil fixed to the target at an intensity of 1×10^{14} W cm^{-2} and wavelength of 527 nm, created an intense x-ray source by pumping the 2 keV Ly-α line in Si[37]. These photons were collimated through a 400 μm diameter aperture in the target, timed to probe the shock as it reached the x-ray collection ports. The x-rays were scattered from the shock front and collected through 400 μm ports at 45° and 135° from the incident photons. The probe pulse was delayed 10-20 ns after the rise of the drive beam, allowing the shock to traverse a distance of 350 μm to reach the volume accessed by the x-ray diagnostic port. The fields of view of the spectrometers were shielded with Ni-coated cones (40° opening angle) from ambient x-ray emission and stray light from both laser beams. The radiation was collected and spectrally dispersed with Highly Ordered Pyrolytic Graphite (HOPG) crystal spectrometers[38] curved at a 107 mm radius.

The drive laser beam used a phase plate to produce a round 600 μm diameter spot on target. The forward scattering measurements were made on deuterium shock-driven by a frequency-doubled 2 ns long laser pulse producing a wavelength of 527 nm at the target. The backscattering measurements were made operating the same laser at the 1054 nm fundamental. These shots used 4 ns drive pulses at moderate compression and 6 ns at higher compression, all at nominal intensities of 4×10^{13} W cm^{-2}.

The drive laser was incident on a CH-coated aluminum layer ranging from 12-40 μm in thickness, depending on intended shock pressure. The CH layer was ablated in the laser-target interaction, driving a shock wave into the Al pusher that released into the D_2 layer. The aluminum shielded the bulk D_2 from hot electrons and x-rays produced in the laser-solid interaction that could preheat the target before the shock arrived.

Since deuterium becomes optically reflective under shock compression, the shock velocity can be directly measured using the velocity interferometry system for any reflector (VISAR) technique[39,40]. For this purpose, we propagated a 532 nm VISAR probe beam anti-parallel to the drive beam along the axis of the shock through the rear window. The reflected signal from the D_2 shock front was collected and sent to two interferometers, coupled to optical streak cameras. These provided two 20 ns long channels showing the evolution of shock velocity on each shot. Using two interferometers of differing sensitivities allowed the absolute velocity to be determined in spite of the discontinuity in phase caused by the shock.

In order to determine the mass density – and hence compression ρ/ρ_0 – of the target using measured shock velocity, one of two approaches is necessary. Impedance matching techniques can be used to determine particle velocity in addition to shock velocity, closing the Rankine-Hugoniot relations[41-43] and directly constraining state variables in the target. Alternatively, existing theoretical models or measured EOS values can be used to calculate compression from the shock velocity measured with VISAR; that is the approach used in this study. While one of several modern EOS models could be effectively used, we have chosen the quotidian equation of state (QEOS)[44] because of its computational efficiency and the fact that it represents a middle ground between popular EOS models in the pressure regime of interest. Because we rely on an EOS that is not perfectly known, this approach requires carefully accounting for that uncertainty in our inferred compression. Hicks and coauthors give a comparison of both calculated and measured EOS values and their associated experimental uncertainties[45]. For our experimental conditions, variations in EOS models are relatively small; near 15 GPa, where we observe the onset of ionization, models vary by about 10% in compression at a given pressure. This uncertainty is included in the error bar of quoted values of mass density (see the Supplementary Information for details).

Figure 3 shows a VISAR streak record along with the extracted shock velocities for high power laser drive conditions. Also shown are simulation results from HYDRA, a radiation-hydrodynamics code widely used for modelling inertial confinement fusion and laser-plasma experiments[46]. HYDRA accurately reproduces the measured late-time shock velocities when scattering is performed. Stray light from the drive beam is visible for 2 ns early in the streak. Shock breakout from the Al pusher into D_2 occurs near the end of the drive beam where a discontinuous fringe shift is visible. As the shock decays, a drop in signal amplitude is visible in the raw data, since reflectivity falls as shock pressure and ionization decrease. The peak velocity immediately following shock breakout from the pusher is 22 km s^{-1} with pressures near 50 GPa, which decays to 14±1 km/s and 15+3.5/-4.5 GPa at 21 ns, the center of the 2 ns long x-ray probe.

Figure 4 shows x-ray scattering spectra from both forward and backward spectrometers. In (A), collective scattering data is shown for two shock conditions: the upper spectrum is taken from the same shot as Figure 3, with a compression of ρ/ρ_0=3.2+0.2/-0.3 at the time of x-ray probing while the lower spectrum used a lower laser intensity drive to reach ρ/ρ_0=2.8+0.3/-0.4.

At this lower drive condition, no inelastic feature is visible above the noise and spectral resolution of the detector, placing an upper bound on ionization state of $Z \leq 0.04$.

At higher drive conditions, a downshifted plasmon feature is visible centered at 1998 eV below the probe energy of E_0=2005 eV. The plasmon resonance in this low-temperature regime experiences very little damping and is therefore quite narrow. The presented fit curves include broadening due to collisional effects calculated in the local-field-corrected Born-Mermin approximation, which goes beyond the random phase approximation to the dynamical structure factor by including electron-electron interactions and electron-ion collisions in the Born approximation[30,47]. The spectrum is convolved with the instrument function introduced by the HOPG crystal and detector. The broad low-energy tail may be explained by bound-free transitions, whose fit includes density and temperature dependent continuum lowering. A best fit to the data indicates a delocalized electron density of $n_e=2.5\pm0.4\times10^{22}$ cm^{-3} due to the free-electron density-sensitive plasmon shift at 7 eV. Combined with the mass density inferred from the VISAR trace, this corresponds to an average ionization state of $Z=0.15\pm0.04$. The measured electron density corresponds to a Fermi temperature of T_F=3.1 eV. For typical temperatures of a fraction of an electron volt, the electrons are therefore strongly degenerate, with $\theta = kT/\varepsilon_F \sim 0.1$, and a scattering parameter of α=1.5.

Figure 5 (A) shows the 135° backscattered spectrum from another shot using a 4 ns laser drive, and a probe beam delay of 15 ns. HYDRA calculations using an intensity profile matched to the velocity measurements shown above predict pressures of 16 GPa and compressions of 3.2+0.2/-0.4, producing target conditions very close to those achieved in the plasmon scattering case. The ratio of elastic to inelastic scattering is strongly dependent on the ionization of the target; with increasing average ionization, the inelastic scattering contribution from free electrons grows relative to the remaining elastic signal. Fits are shown for ionizations Z=0.1-0.5 and a best fit is achieved for $n_e=2.4\times10^{22}$ cm^{-3}. This corresponds $Z=0.15\pm0.08$, in good agreement with the plasmon data. At these conditions, the scattering parameter is α=0.63.

Discussion

For non-collective scattering, the theoretical models used to describe the bound-free contribution can have a significant effect on the inelastic spectrum. In the present case where weakly bound electrons in the compressed deuterium occupy states near the continuum,

continuum depression plays a particularly important role. To minimize any ambiguity introduced by this model dependence, we have compared our results, which use a Stewart-Pyatt (SP) model[48] for ionization potential depression (IPD), with a set of calculations using the Eckert-Kröll (EK)[49] model. The resulting curves are shown in Figure 5 (B), with the SP model in red and the EK model in blue. The contribution to the spectrum from bound-free scattering are shown separately as dashed curves, illustrating that the primary difference comes through the shift of the EK feature toward E_0. We attribute this to a much higher value of continuum depression calculated by the EK model, ΔE_{EK}=10.2 eV compared to ΔE_{SP}=2.1 eV for SP. We note that in both cases a best fit is found for an ionization state of Z=0.15. We conclude that, for very similar experimental drive conditions, plasmon and Compton scattering provide nearly identical ionization states; this is significant because the sensitivity of plasmon spectra and Compton scattering spectra to bound-free models and structure factors is very different. This finding indicates that contributions from bound-free scattering and interband transitions are accounted for by our data analysis and that interband transitions play a minor role in the interpretation of the data.

Figure 6 summarizes measurements of ionization across several shock-drive and probe delay conditions producing compressions between ρ/ρ_0=2.8 and ρ/ρ_0=4.05. Measured ionization states for both forward and backscattered configurations are shown as a function of compression, along with predicted ionizations from several models. The compression values for the backscattering data points and the lowest compression case, where velocity measurements are not possible below the onset of optical reflectivity, were determined using hydrodynamic calculations benchmarked to VISAR measurements. The error bars in compression for these points include a 20% uncertainty in drive intensity and uncertainty between EOS models at the relevant pressures. The data indicate a sharp onset of ionization between 3 and 3.5 times compression.

This onset is reproduced by average-atom simulations of a D ion system embedded in a plasma background[50], but with lower absolute ionization values. The Thomas-Fermi model exhibits very little of the density dependence in the data at low compression. Similar results have been reported in x-ray scattering experiments on shock-compressed CH[51]. We also show the deuterium dissociation curve calculated with the code FVT, a chemical picture model based on fluid variational theory[52] that predicts the onset of molecular dissociation at higher compressions than measured here.

Theoretical models for dense matter can be divided into chemical and physical picture models. In the chemical picture, ions, atoms and molecules are treated as elementary members of the ensemble, while in the physical picture, nuclei and electrons are treated as elementary particles and bound states are long-lived correlations between them. While ab initio physical picture theories represent the state-of-the-art in simulating hydrogen under extreme conditions, an explicit definition of ionization within a physical-picture model is difficult in pressure and temperature regimes where electron delocalization and finite temperatures blur the characteristics of free and bound electrons. To provide a comparison to our measurements we have calculated the dissociation of deuterium molecules along the Hugoniot using DFT-MD[53]. DFT-MD couples a finite-temperature treatment of electrons using density functional theory with a molecular dynamics treatment of ion motion. The dissociated fraction, shown in red in Figure 6, is estimated by tracking neighboring ions in the system as the simulation evolves in time; the method is described in more detail in the Supplementary Information. The fraction of dissociated molecules in the calculations matches the fraction of measured ions closely, suggesting that the processes of dissociation and ionization occur nearly simultaneously along the Hugoniot, see also Refs. 21-23.

In order to facilitate further comparison between our simulations and experimental results, optical reflectivity and dynamic conductivity were calculated from the DFT-MD results. Figure 7 (A) shows reflectivity calculated along the principal Hugoniot. Comparisons are made at 808 nm with the results of Celliers[7] and at 532 nm with the recent measurements by Loubeyre and coworkers[54]. Good agreement is found between experiment and theory. Between 20-50 GPa, DFT-MD is seen to produce somewhat higher reflectivities than the Loubeyre results, attributable to the fact that DFT-MD underestimates the band gap systematically using exchange-correlation functionals like PBE[55], leading to early band gap closure and an earlier onset of dissociation and, thereby, conduction. In Figure 7 (B), the dynamic conductivity along the Hugoniot is plotted at a pressure range corresponding to our experimental conditions. The DC limit is plotted in the inset, showing that conductivity starts at very small values near 0.1 S m^{-1} at 2.8x compression (black curve), rising orders of magnitude to a metallic conductivity of 10^5 S m^{-1} near fourfold compression (yellow curve). This confirms the continuous transition from an insulating molecular fluid to a metallic degenerate electron liquid observed in the experiments.

More broadly, this work demonstrates the viability of combining x-ray spectroscopic and optical velocity measurements to make detailed inferences into the electronic states of a variety of materials compressed to pressures relevant to planetary science. As fourth-generation light sources come online, we expect these results to lead to an unprecedented exploration of the high-pressure structure of hydrogen and other light elements and allow experimental determination of such properties as interior temperature profiles and core erosion in giant planets.

References:

1. Wigner, E. & Huntington, H. B. On the possibility of a metallic modification of hydrogen. *J. Chem. Phys*. **3**, 764-770 (1935).
2. Guillot, T. Interiors of giant planets inside and outside the solar system. *Science* **286**, 72-77 (1999).
3. Nettelman, N., Holst, B., Kietzmann, A., French, M. & Redmer, R. Ab initio equatio of state data for hydrogen, helium, and water and the internal structure of Jupiter. *Astrophys. J.* **683**, 1217-1228 (2008).
4. Wilson, H.F. & Militzer, B. Rocky Core Solubility in Jupiter and Giant Exoplanets. *Phys. Rev. Lett*. **108**, 111101 (2012).
5. Nellis, W. J., Weir, S. T. & Mitchell, A. C. Metallization and electrical conductivity of hydrogen in Jupiter. *Science* **273**, 936-938 (1996).
6. Vorberger, J., Tamblyn, I., Militzer, B. & Bonev, S. A. Hydrogen-helium mixtures in the interiors of giant planets. *Phys. Rev. B* **75**, 024206 (2007).
7. Loubeyre, P., Occelli, F. & LeToullec, R. Optical studies of solid hydrogen to 320 GPa and evidence for black hydrogen. *Nature* **416**, 613–617 (2002).
8. Eremets, M. I. & Troyan, I. A. Conductive dense hydrogen. *Nat. Mater.* **10**, 927-931 (2011).
9. Eremets, M. I., Troyan, I. A., Lerch, P. & Drozdov, A. Infrared study of hydrogen up to 310 GPa at room temperature. *High Pressure Research* **33**, 377-380 (2013).
10. Zha, C. S., Liu, Z. & Hemley, R. J. Synchrotron Infrared Measurements of Dense Hydrogen to 360 GPa. *Phys. Rev. Lett.* **108**, 146402 (2012).
11. Zha, C., Cohen, R. E., Mao, H., Hemley, R. J. Raman measurements of phase transitions in dense solid hydrogen and deuterium to 325 GPa. *Proc. Nat. Acad. Sci. USA* **111**, 4792–4797 (2014).
12. Cohen, R. E., Naumov, I. I. & Hemley, R. J. Electronic excitations and metallization of dense solid hydrogen. *Proc. Nat. Acad. Sci. USA* **110**, 13757–13762 (2013)
13. Howie, R. T., Guillaume, C. L., Scheler, T., Goncharov, A. F. & Gregoryanz, E. Mixed molecular and atomic phase of dense hydrogen. *Phys. Rev. Lett*. **108**, 125501 (2012).
14. McMahon J.M., Morales M.A., Pierleoni C. & Ceperley D.M.. The properties of hydrogen and helium under extreme conditions. *Rev Mod Phys.* **84**, 1607–1653 (2012).

15. Weir, S. T., Mitchell, A. C. & Nellis, W. J. Metallization of fluid molecular hydrogen at 140 GPa (1.4 Mbar). *Phys. Rev. Lett.* **76**, 1860 (1996).
16. Nellis, W. J., Weir, S. T. & Mitchell, A. C. Minimum metallic conductivity of fluid hydrogen at 140 GPa (1.40 Mbar). *Phys. Rev. B* **59**, 3434-3449 (1999).
17. Nellis, W. J. Wigner and Huntington: the long quest for metallic hydrogen. *High Pressure Research* **33**, 369-376 (2013).
18. Knudson, M. D, *et al*. Direct observation of an abrupt insulator-to-metal transition in dense liquid deuterium. *Science* **348**, 1455-1460 (2015).
19. Celliers, P. M. *et al.* Shock-Induced Transformation of Liquid Deuterium into a Metallic Fluid. *Phys. Rev. Lett.* **84**, 5564 (2000).
20. Regan, S. *et al*. Inelastic X-Ray Scattering from Shocked Liquid Deuterium. *Phys. Rev. Lett.* **109**, 265003 (2012).
21. Lorenzen, W., Holst, B. & Redmer, R. First-order liquid-liquid phase transition in dense hydrogen. *Phys. Rev. B.* **82**, 195107 (2010).
22. Morales, M. A., Pierleoni, C., Schwegler, E. & Ceperley, D. M. Evidence for a first-order liquid-liquid transition in high-pressure hydrogen from ab initio simulations. *Proc. Nat Acad. Sci. USA* **107**, 12799-12803 (2010).
23. French, M. *et al. Ab initio* simulations for the material properties along Jupiter's adiabat. *Astrophys. J. Suppl. Ser.* **202**, 5 (2012).
24. Gastine, T., Wicht, J., Duarte, L .D. V., Heimpel, M. & Becker, A. Explaining Jupiter's magnetic field and equatorial jet dynamics. *Geophys. Res. Lett*. **41,** 5410 (2014).
25. Caillabet, L., Mazevet, S. & Loubeyre, P. Multiphase equation of state of hydrogen from ab initio calculations in the range 0.2 to 5 g/cc up to 10 eV. *Phys. Rev. B* **83,** 094101 (2011).
26. Becker, A., Lorenzen, W., Fortney, J. J., Nettelmann, N., Schöttler, M. & Redmer, R. Ab initio equations of states for hydrogen (H-REOS.3) and helium (He-REOS.3) and their implications for the interiors of brown dwarfs. *Astrophys. J. Suppl. S.* **215,** 21 (2014).
27. Tamblyn I. & Bonev, S. A.. Structure and phase boundaries in compressed liquid hydrogen. *Phys. Rev. Lett.* **104,** 065702 (2010).
28. Glenzer, S. H. & Redmer, R. X-ray Thomson scattering in high energy density plasmas. *Rev. Mod. Phys*. **81**, 1625-1663 (2009).

29. Kritcher, A. L. *et al.* Ultrafast X-ray Thomson Scattering. *Science* **322**, 69-71 (2008).
30. Neumayer, P. *et al.* Plasmons in Strongly Coupled Shock-Compressed Matter. *Phys. Rev. Lett.* **105**, 075003 (2010).
31. Fortmann, C. *et al.* Measurement of the heat capacity ratio in shock compressed Be. *Phys. Rev. Lett.* **108**, 175006 (2012).
32. Garcia-Saiz, E. *et al*. Probing warm dense lithium by inelastic X-ray scattering. *Nat. Phys* **4**, 940-944 (2008).
33. Chihara, J. Interaction of photons with plasmas and liquid metals – photoabsorption and scattering. *J. Phys.: Condens. Matter* **12**, 231 (2000).
34. Gregori, G., Glenzer, S. H., Rozmus, W., Lee, R. W. & Landen, O. L. Theoretical model of x-ray scattering as a dense matter probe. *Phys. Rev. E* **67**, 026412 (2003).
35. Glenzer, S. H. *et al.* Observations of Plasmons in Warm Dense Matter. *Phys. Rev. Lett*. **98**, 065002 (2007).
36. Glenzer, S. H. *et al*. Demonstration of Spectrally Resolved X-Ray Scattering in Dense Plasmas. *Phys. Rev. Lett*. **90**, 175002 (2003).
37. Davis, P., Döppner, T., Glenzer, S. H., Falcone, R. W. & Unites, W. An apparatus for the characterization of warm, dense deuterium with inelastic x-ray scattering. *JINST* **7**, 02004 (2012).
38. Pak, A. *et al*. X-ray line measurements with high efficiency Bragg crystals. *Rev. Sci. Inst.* **75**, 3747-3749 (2004).
39. Celliers, P. M. *et al.* Line-imaging velocimeter for shock diagnostics at the OMEGA laser facility. *Rev. Sci. Inst.* **75**, 4916-4929 (2004).
40. Falk, K. *et al.* Comparison between x-ray scattering and velocity-interferometry measurements from shocked liquid deuterium. *Phys. Rev. E* **87**, 043112 (2013).
41. Collins, G. W. *et al.* Measurements of the Equation of State of Deuterium at the Fluid Insulator-Metal Transition. *Science* **281**, 1178-1181 (1998).
42. Knudson, M. D. *et al.* Equation of State Measurements in Liquid Deuterium to 70 GPa. Phys. Rev. Lett. **87**, 225501 (2001).
43. Knudson, M. D. *et al.* Principal Hugoniot, reverberating wave, and mechanical reshock measurements of liquid deuterium to 400 GPa using plate impact techniques. *Phys. Rev. B* **69**, 144209 (2004).

44. More, R. M., Warren, K. H., Young, D. A. & Zimmerman, G. B. A new quotidian equation of state (QEOS) for hot dense matter. *Phys. Fluids* **31**, 3059-3078 (1988).
45. Hicks, D. G. *et al.* Laser-driven single shock compression of fluid deuterium from 45 to 220 GPa. *Phys. Rev. B* **79**, 014112 (2009).
46. Marinak, M. M. *et al.* Three-dimensional simulations of Nova high growth factor capsule implosion experiments. *Phys. Plasmas* **3**, 2070 (1996).
47. Redmer, R., Reinholz, H., Röpke, G., Thiele, R. & Höll, A. Theory of X-Ray Thomson Scattering in Dense Plasmas. *IEEE Trans Plasma Sci* **33**, 77-84 (2005).
48. Stewart, J. C. and Pyatt Jr., K. D. Lowering of Ionization Potentials in Plasmas *Astrophys. J.* **144**, 1203 (1966).
49. Ecker, G. and Kröll, W. Lowering of the Ionization Energy for a Plasma in Thermodynamic Equilibrium. *Phys. Fluids* **6**, 62 (1963).
50. Johnson, W. R., Guet, C. & Bertsch, G. F. Optical Properties of Plasmas Based on an Average-Atom Model. *J. Quant. Spect. Rad. Trans.* **99**, 327 (2006).
51. Fletcher, L. B. *et al.* Observations of Continuum Depression in Warm Dense Matter with X-Ray Thomson Scattering. *Phys. Rev. Lett.* **112**, 145004 (2014).
52. Holst, B., Nettelmann, N. & Redmer, R. Equation of State for Dense Hydrogen and Plasma Phase Transition. *Contrib. Plasma Phys.* **47**, 368-374 (2007).
53. Holst, B., Redmer, R. & Desjarlais, M. P. Thermophysical properties of warm, dense hydrogen using quantum molecular dynamics simulations. *Phys. Rev. B* **77**, 184201 (2008).
54. Loubeyre, P. *et al.* Extended data set for the equation of state of warm dense hydrogen isotopes. *Phys. Rev. B*, **86**, 144115 (2012).
55. Perdew, J. P., Burke, K. & Ernzerhof, M. Generalized gradient approximation made simple. *Phys. Rev. Lett*. **77**, 3865 (1996).

Acknowledgements: This work performed under the auspices of the (U.S.) Department of Energy (DOE) by Lawrence Livermore National Laboratory (LLNL) under Contract No. DE-AC52- 07NA27344 and supported by Laboratory Directed Research and Development (LDRD) grant 11-ER- 050. SLAC HED science is supported by DOE Office of Science, Fusion Energy Science under FWP 100182. P.D. was supported by the NNSA SSGF program. A.B., B.H., P.S., and R.R. acknowledge support from the Deutsche Forschungsgemeinschaft (DFG) within the SFB 652 and the BMBF via the FSP-301. A.B. performed calculations within the grant mvp00008 at the North-German Supercomputing Alliance (HLRN).

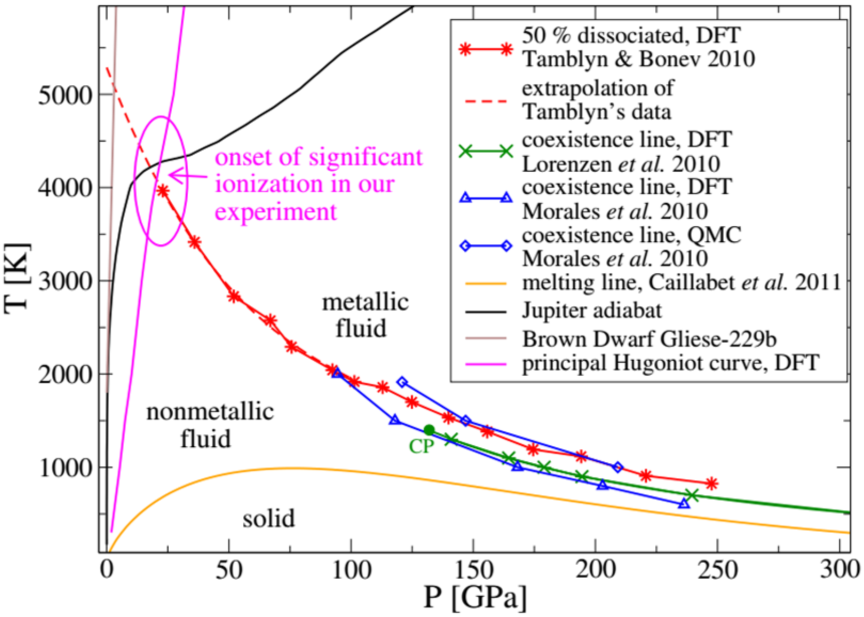

Fig. 1: Phase diagram of hydrogen. Displayed are the melting line[25] (orange), the isentropes of Jupiter[2,23] (black) and the Brown Dwarf Gliese-229b[26] (brown), the principal Hugoniot curve (magenta), and results for the first-order liquid-liquid (plasma phase) transition (green[21], blue[22]) together with predictions at which P - T points the system is dissociated by 50%[27] (red).

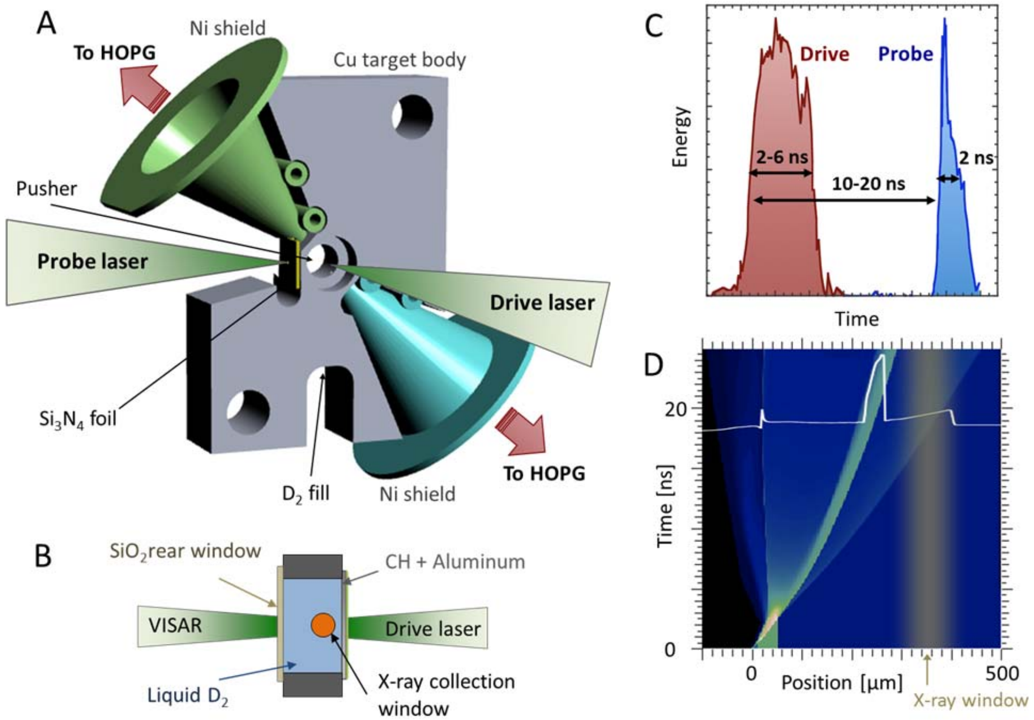

Fig. 2: Experimental setup and timing. **(A)** The copper target is held at 19 K, liquefying the deuterium that is filled into the central cavity. A drive laser is incident on a 2 mm diameter Al pusher, launching a shock wave along the axis. A probe laser irradiates a Si_3N_4 foil, pumping the 2005 eV Si Ly-α transition. X-rays scattered in the forward and backward directions are spectrally dispersed with highly-oriented pyrolytic graphite (HOPG) crystals whose direct view of the laser-plasma is prevented by Ni shields. **(B)** Cross section of the target reservoir across the thickness of the target. The target is sealed with aluminum on the front surface and a transparent quartz rear window to allow the VISAR beam to probe shock evolution. **(C)** Schematic of laser beam timing showing the shock drive beam (red) of 2-6 ns preceding a 2 ns probe pulse. The probe was delayed by 10-20 ns, depending on drive intensity, to allow the shock front to advance into the x-ray spectrometer view. Shorter delay times yielded higher shock pressures. **(D)** HYDRA simulations of mass density evolving as a function of space and time, with a lineout at the x-ray probe time of 20 ns. The compressed D_2 peak (ρ_{Shock}=0.54 g cm^{-3}) has traversed into the spectrometer field of view at t=20 ns when we make the x-ray measurement. The high-density peak lagging the D_2 shock front is due to the aluminum pusher, but is shielded by the x-ray window.

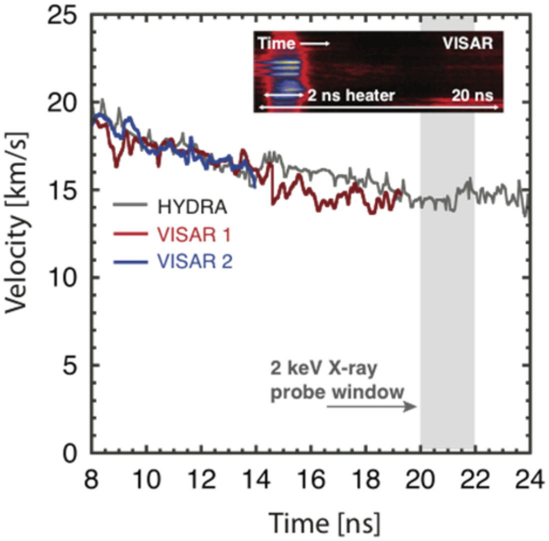

Fig. 3: VISAR shock velocity compares well with hydrodynamic simulations up to 20 ns when the x-ray probe begins. We linearly extrapolate the mean velocity to obtain the average conditions during the x-ray probe. Uncertainty in shock velocity is estimated to be ±1 km/s; uncertainty in timing is ±0.5 ns. Inset: Raw VISAR streak for one of two streak cameras. The bright pulse early in time comes from the drive beam. Breakout of the shock from the aluminum pusher into the deuterium occurs near the end of the drive beam, and the decaying shock velocity in D_2 is extracted from the fringes shifting in time.

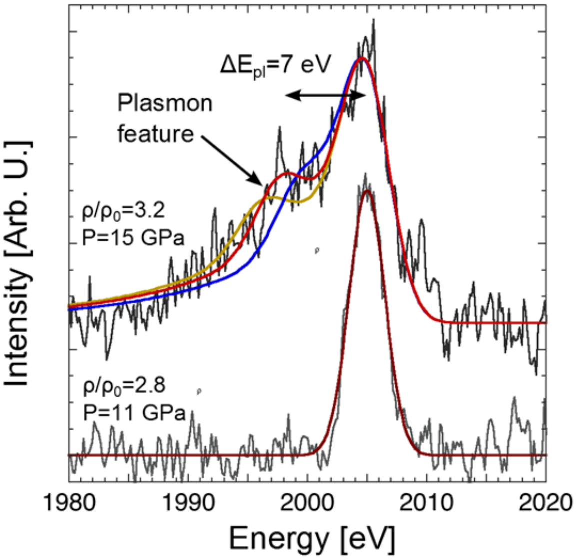

Fig. 4: Measured x-ray scattering spectra with theoretical fits. Pressure and compression are inferred from VISAR measurements. X-ray forward scattering spectrum from 3.2x shock-compressed D_2 showing elastic scatter at 2005 eV and downshifted plasmon with theoretical fits corresponding to T_e=0.15 eV and n_e=1.3(blue), 2.5 (red) and 4.0 (yellow) $\times 10^{22}$ cm^{-3}. Below, a spectrum from 2.8x compressed D_2 showing no evidence of free electrons as a visible inelastic scattering feature.

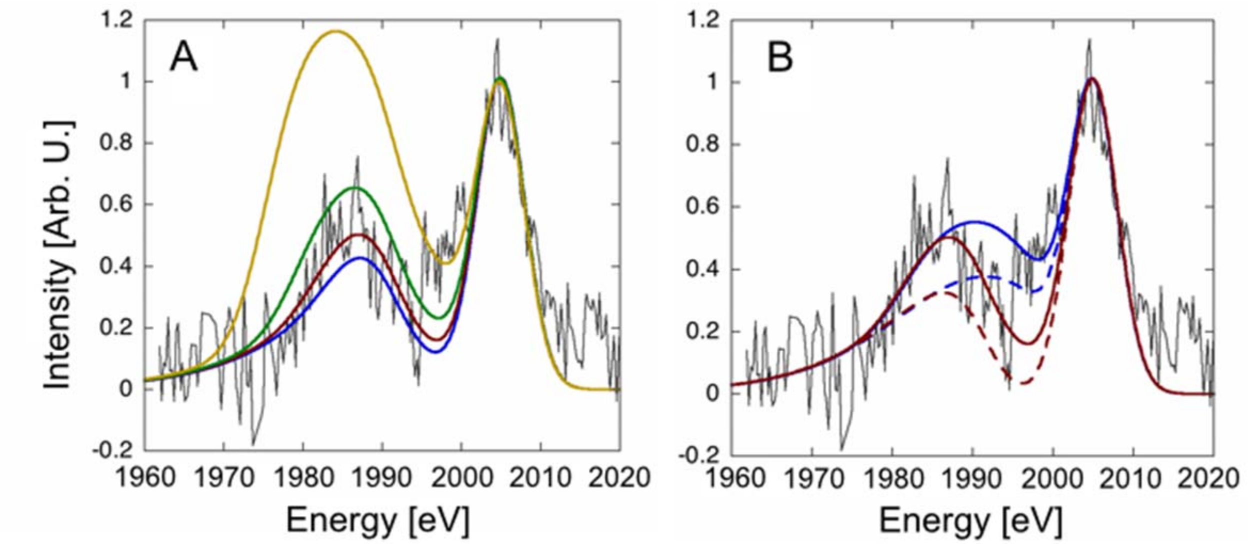

Fig. 5: Backscattering spectra with theoretical fits for target conditions of Te=0.15 eV and ρ/ρ0=3.2. **(A)** Four ionization states corresponding to Z=0.1 (blue), 0.15 (red), 0.25 (green) and 0.5 (yellow) are shown, with a best fit found for $n_e=2.4\times10^{22}$ cm^{-3} and Z=0.15±0.08. **(B)** Theoretical fits for Z=0.15 using Stewart-Pyatt (red) and Ecker-Kröll (blue) models for ionization potential depression. Solid lines correspond to the total spectrum and dashed to the elastic and bound-free scattering contributions without free-free scattering. Both models result in best fit values for ionization of Z=0.15.

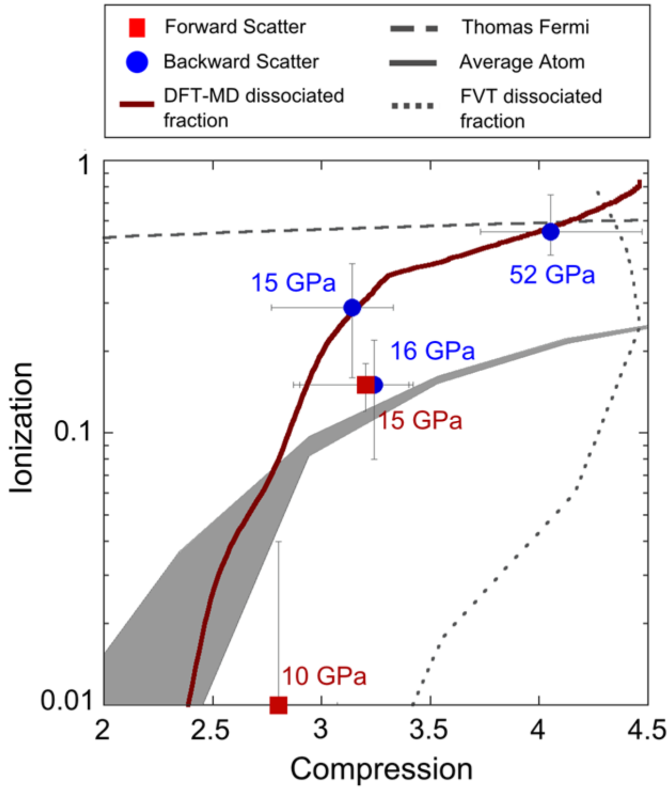

Fig. 6: Average ionization of D_2 plotted as a function of compression along the single shock Hugoniot. Values of ionization inferred from plasmon measurements are shown as red squares, measurements using Compton scattering are shown as blue circles, and pressures from QEOS are indicated for each data point. Ionization degree calculated with Thomas-Fermi theory is shown as a dashed line, while average-atom calculations are shown between a lower bound of T_e=0.1 eV and an upper bound of T_e=0.5 eV as a shaded region. The dark red line shows the molecular dissociation fraction calculated from density functional molecular dynamics simulations along the principal Hugoniot and the dotted line shows a similar dissociation calculation with the chemical picture code FVT. Measurements indicate a sharp increase in ionization near 3× compression, consistent with the DFT-MD calculated dissociated fraction.

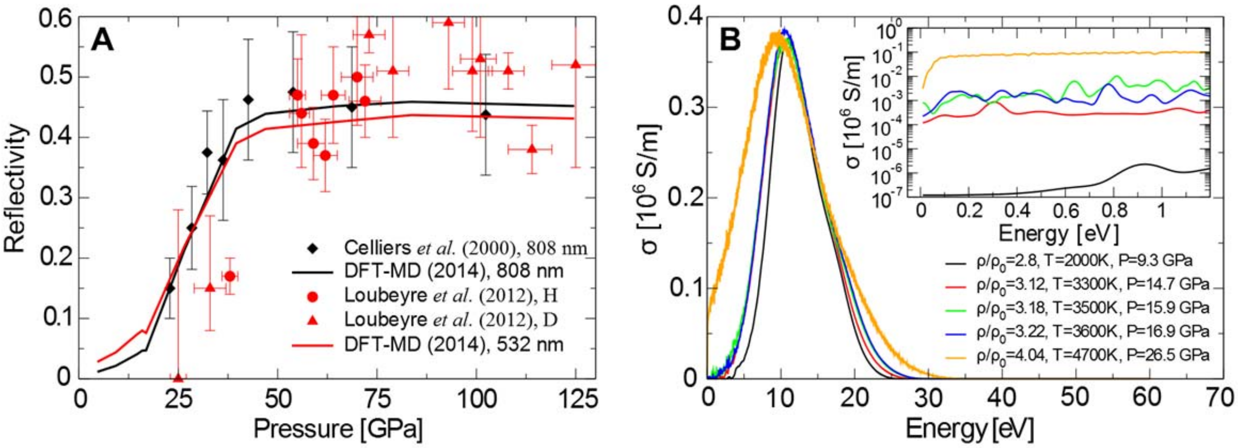

Fig. 7: (A) Reflectivities along the principal Hugoniot curve for 808 nm from the experiments of Celliers et al. (black diamonds) and DFT-MD calculations in this work (solid black line). Reflectivities for 532 nm from the experiments of Loubeyre et al. in hydrogen (red dots) and deuterium (red triangles) and DFT-MD calculations in this work (solid red line). **(B)** Dynamic electrical conductivity at the five experimental points for which the thermodynamic states along the principal Hugoniot curve are given in the legend. The dc limit (ω → 0) is displayed in the inset.

Supplementary information: Dissociation-induced metallization of dynamically compressed deuterium

P. Davis[1,2*], , T. Döppner[2], J.R. Rygg[2], C. Fortmann[2,3], L. Divol[2], A. Pak[2], L. Fletcher[4], A. Becker[5], B. Holst[5], P. Sperling[5], R. Redmer[5], M.P. Desjarlais[6], P. Celliers[2], G.W. Collins[2], O.L. Landen[2], R.W. Falcone[1], S.H. Glenzer[4]

[1]University of California, Berkeley, Berkeley, CA 94709, USA
[2]Lawrence Livermore National Laboratory, PO Box 808, Livermore, CA 94551, USA
[3]University of California, Los Angeles, Los Angeles, CA 90095, USA
[4]SLAC National Accelerator Laboratory, CA 94025, USA
[5]Institut für Physik, Universität Rostock, D-18051 Rostock, Germany
[6]Sandia National Laboratories, Albuquerque, NM 87185, USA

SI. I. EXPERIMENTAL METHODS AND MATERIALS

The experiments were performed at the Janus Laser Facility, at Lawrence Livermore National Laboratory. The experimental configuration is illustrated in Figure 2 of the main text. A copper target held a reservoir of liquid deuterium near 19 K with initial deuterium density of ρ_0=0.17±0.004 g/cm^3. A single laser beam drove a shock into the deuterium with intensities of ~4×10^{13} W/cm^2 at the target in 2-6 ns long pulses. The beam used a phase plate to produce a round 600 μm diameter spot on target. The forward scattering measurements were made on deuterium shock-driven by a frequency-doubled 2 ns long laser pulse producing a wavelength of 527 nm at the target. The backscattering measurements were made operating the same laser at the 1054 nm fundamental, leading to higher intensities on target. These shots used pulses of up to 6 ns to sustain higher-pressure shocks in the target.

A second 527 nm beam was propagated at 90° to the drive beam, incident on a Si_3N_4 foil with an intensity of 1×10^{14} W/cm^2. This beam pumped the Si Ly-α line at 2005 eV, producing a bright x-ray source of bandwidth $\delta E/E=2\times10^{-3}$, sufficiently narrow to observe small plasmon shifts at fractional ionizations *(S1)*. The probe pulse was delayed 10-20 ns after the rise of the drive beam, allowing the shock to traverse a distance of 350 μm to reach the center of the volume accessed by the x-ray diagnostic port. Conversion efficiency of laser energy into the Ly-α line was measured to be 0.2%, producing approximately 4×10^{12} x-ray photons at the target, sufficient for accurate single-shot measurements.

The x-rays were dispersed with Highly Ordered Pyrolytic Graphite (HOPG) crystal spectrometers, 24 x 70 mm curved with a radius of curvature (ROC) of 107 mm. The spectrometers operated in von Hamos geometry *(S2)* collected and spectrally dispersed the scattered radiation onto Fuji BAS-TR025 image plates, resulting in a dispersion of 3.5 eV/mm and 4 eV instrument functions. The image plates were scanned at a resolution of 50 μm. The soft x-ray bremsstrahlung produced by the laser-target interaction was filtered by a 25 μm thick Be foil or a layer of aluminized plastic a few μm thick that was placed in front of the image plate. Of the ~4×10^{12} photons produced, a fraction of 7×10^{-4} photons were scattered on a typical shot, consistent with the electron densities ~4×10^{22} cm^{-3} measured at fractional ionizations. Figure S1 shows the x-ray source function as measured with the HOPG and image plates.

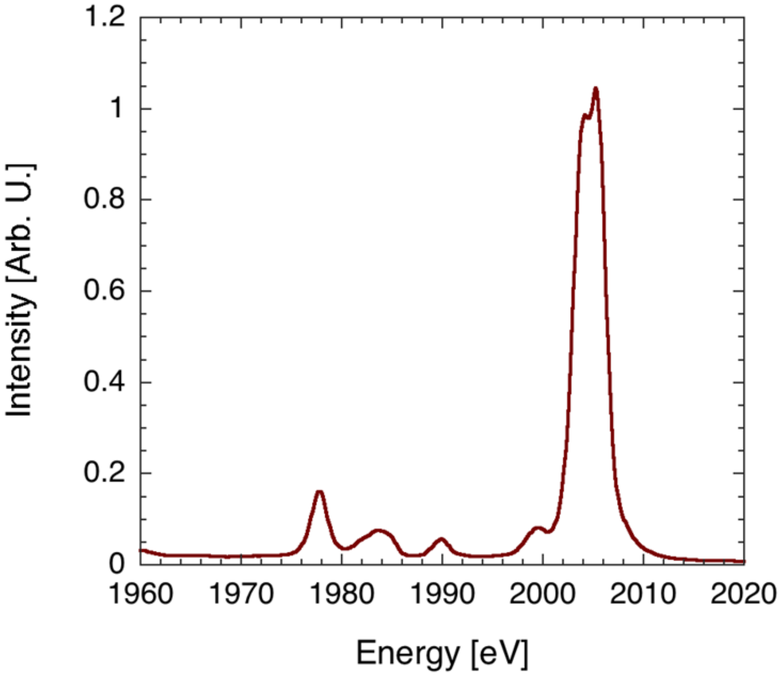

FIGURE S1: Si Li-α x-ray source function as measured with HOPG crystal spectrometer and image plates.

In dynamic x-ray scattering experiments, contributions from unshocked material can contaminate the desired signal from the shocked sample. In our case, we note that the x-ray aperture is sufficiently small to localize the measurement to a volume mostly constrained to the shock front. This is further weighted by the higher scattering contribution from dense, hot material to confine the measurable signal to the shocked matter. We performed null tests on undriven targets to verify that there was no significant contribution from the target or unshocked volume. In addition, the plasmon data do not have the broadening or lower energy shifts we would expect from scattering from lower density hydrogen, and we are thus confident that our signal is collected from the compressed volume.

The mixing of pusher material into the field of view of the spectrometer would also be an important failure mode. However, we would expect this to be detectable as a spuriously large electron density and as a larger total photon signal at the detector. Neither signature was evident in our data.

Falk and coauthors have raised questions about combining VISAR measurements from a shock front with spatially integrated XRTS in similar experiments, particularly in the presence of gradients in plasma conditions *(S3).* While this is an important point, we note that the Falk experiment was designed to maximize scattering signal by scattering from a large volume of the target with an x-ray source antiparallel to the drive beam and thus including significant contributions from coronal plasma and all other plasma conditions present. We have attempted to control this with a narrower x-ray aperture. The Falk geometry also necessitated a design that did not use a solid density pusher on the target surface. As a result, Falk et al. report less uniform shock conditions than would otherwise be obtained, as well as measurable target preheat. We have avoided this outcome with an experimental design that allows for the use of an Al pusher. Significant variations in electron density would be expected to broaden the plasmon signal measurably and result in a less shifted spectral feature – something we do not detect in our data.

SI. II. X-RAY SCATTERING ANALYSIS

The recorded x-ray spectra were fit with a theoretical model that includes the spectral contributions of ions, free electrons and bound electrons. The model is based on the Chihara formula,

$$S(k,\omega)=\left|f_I(k)+q(k)\right|^2 S_{ii}(\mathrm{k})+Z_f S_{ee}(k,\omega)+Z_c\int S_{CE}(k,\omega-\omega')S_S(k,\omega')d\omega'$$

This formula describes the scattering spectrum as a combination of elastic scattering (first term), inelastic scattering from delocalized electrons (second term) and inelastic scattering from weakly bound electrons, including bound-free transitions to the continuum. Z_f and Z_c denote the number of delocalized (free) and weakly bound core electrons respectively.

The first term accounts for density correlations of electrons that follow the ion motion, including core electrons (represented by the ion form factor $f(k)$) and the screening electrons ($q(k)$). At the instrument resolutions obtained in our study, the ion-ion correlation function $S_{ii}(k,\omega)$ can be approximated $S_{ii}(k,\omega) = S_{ii}(k)\delta(\omega)$. The static ion structure factor is calculated in the Debye-Hückel approximation *(S4)*.

The second term describes the density correlations of free electrons. This term is often calculated in the random phase approximation (*RPA*), which assumes weak inter-particle interactions. Improvements have been introduced to account for strong coupling effects in dense matter in the form of the Born-Mermin approximation (*BMA*) *(S5)*. This approach introduces a dynamic collision frequency $v(\omega)$ using an ansatz suggested by Mermin *(S6)*. The collision frequency is calculated in the Born approximation *(S7)*. Further improvements have been made by introducing local field corrections (*LFC*) *(S8)*. Together, this *BMA-LFC* approach was shown to greatly improve the description of plasmon dispersion in warm, dense matter *(S9)*. We use it in all of our analysis, although tests against *RPA* calculations show that the two models do not differ significantly at the density and temperature conditions explored in our study.

The third term describes bound-bound and bound-free scattering processes through the term $S_{CE}(k,\omega)$. There has been much recent work to improve the theoretical description of this term *(S10-S12)*, which introduces significant model-dependence into the inelastic spectrum. In our case, we are primarily concerned with the treatment of ionization potential depression (IPD) which can introduce plasma-parameter-dependent energy shifts and changes in shape to the bound-free component of the spectrum. In order to minimize the ambiguity of our fits, we compare calculations using two different models for IPD - the Stewart-Pyatt (SP) *(S13)* and Ecker-Kröll (EK) *(S14)* approaches. The results are plotted in Figure S2.

In Figure S2 (A), we show SP fits for ionizations of Z-0.15, 0.25 and 0.5 (solid lines) as well as dotted lines for those conditions representing only the bound-free and elastic scattering contributions. All fits were calculated for T_e=0.15 eV and ρ/ρ_0=3.2. Relative to the elastic scattering feature, the free-free scattering contribution grows much more rapidly with increasing ionization than the bound-free component. While IPD models affect the overall shape of the inelastic feature, this weak-scaling of the bound-free component with density means it has only a limited effect on the electron density inferred from the measurement. A best fit of Z=0.15 is found.

In Figure S2 (B), we show EK fits for the same conditions and ionizations of Z=0.15 and 0.25. Dotted lines again correspond to bound-free and elastic scattering. In this case the peak of the bound-free feature is shifted toward E_0 relative to the SP case, a result we attribute to the much larger calculated lowering of the continuum in the case, ΔE_{EK}=10.2 eV compared with ΔE_{SP}=2.1 eV in the Stewart-Pyatt case. Nevertheless, we find Z=0.15 fits the spectrum best. The agreement in calculated density between these two cases gives us confidence that our inferred electron density is correct, notwithstanding the model-dependence of the bound-free feature.

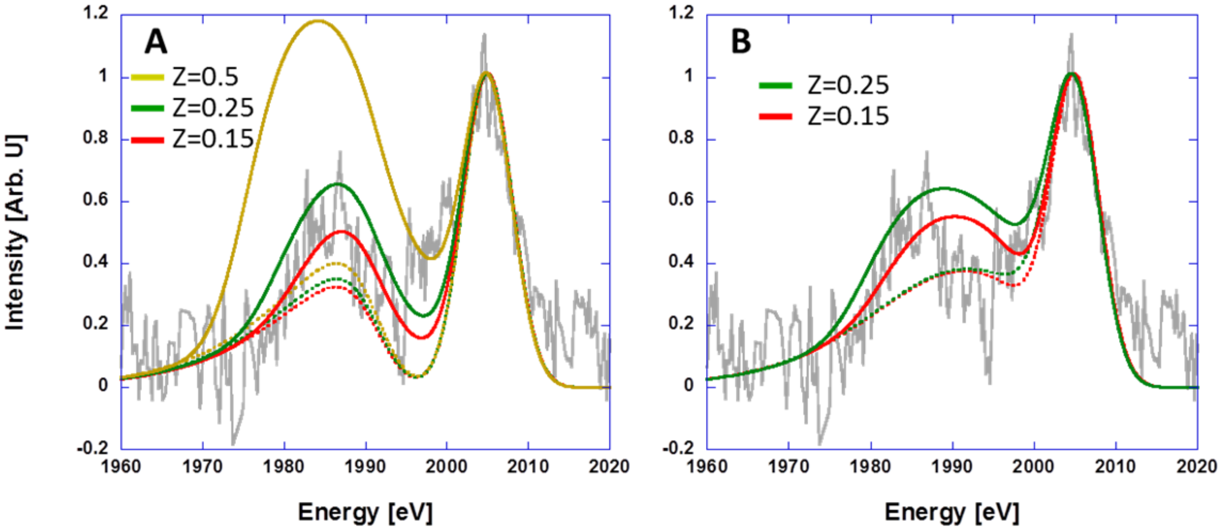

Figure S2: Backscattering spectra and fits using two models for ionization potential depression (IPD). Solid curves represent the total scattering signal while dashed lines indicate contributions from bound-free and elastic scattering only. (A) Stewart-Pyatt IPD model for ionizations of Z=0.15 (red), 0.25 (green) and 0.5 (yellow). (B) Ecker-Kröll results for Z=0.15 (red) and 0.25 (green). 8 eV more continuum lowering effectively results in a shift of the bound-free scattering feature toward the elastic peak.

We also tested the temperature dependence of the spectrum and found a very weak dependence in the intensity of the inelastic feature relative to the elastic. This is illustrated in Figure S3 (A), where fits are shown for T_e=0.15, 0.25 and 0.5 eV at Z=0.15 and ρ/ρ_0=3.2. Because the scattering intensity is not a sensitive function of temperature, our stated T_e=0.15 eV measurement is only a rough estimate, albeit one that is consistent with forward scattering. Consequently, Compton scattering is only sensitive to Z; uncertainties in T_e do not affect the quoted values for Z.

Figure S3 (B) shows the plasmon scattering data from Figure 4 of the main text with fits corresponding to Z=0.15 and temperatures of T_e=0.1, 0.15 and 0.2 eV. In this case, it is found that the intensity of the elastic feature changes with temperature relative to the plasmon feature, but that the spectral location of the plasmon feature is temperature insensitive. This is to be expected at such low temperatures, where the thermal correction to the plasmon dispersion relation is too small to play a role. As a result, we are confident that the downshifted plasmon energy is a robust, first-principles measure of electron density.

The static structure factor of dense plasmas, particularly at small k-values in forward scattering experiments, remains an important and challenging research problem *(S15)*. Our fits at T_e=0.15 eV are presented only as rough estimates that are model dependent, and are somewhat lower than the DFT-MD results of order ~0.3 eV at this point on the Hugoniot. However, the inferred ionization is insensitive to variations in temperature and consistent between the very different forward and backward scattering regimes.

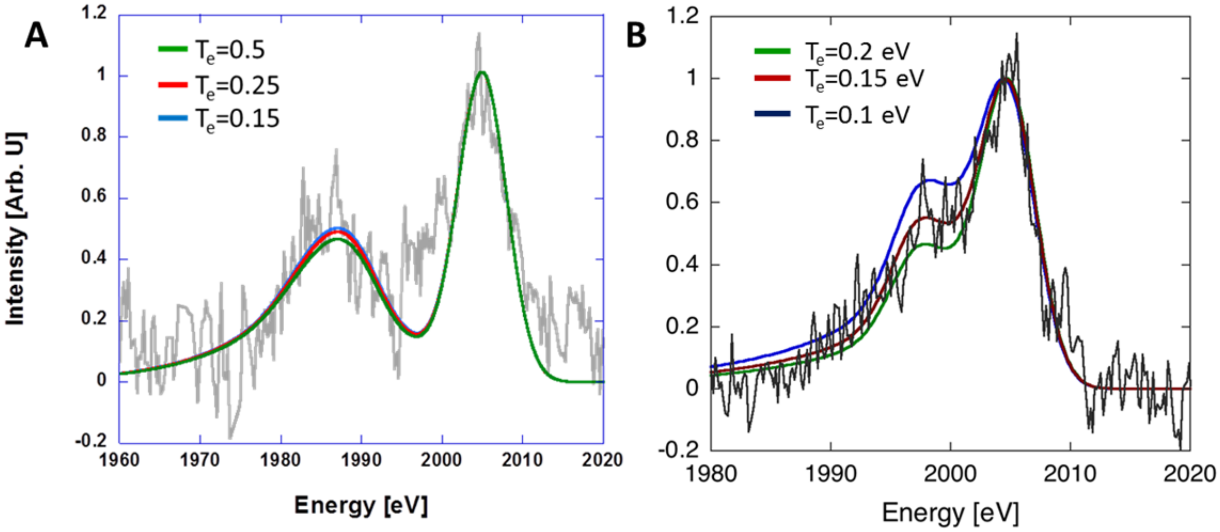

FIGURE S3: Temperature dependence of x-ray scattering fits. (A) Backscattering data fit with three temperatures at Z=0.15. Very little change is seen for fits ranging from T_e=0.15-0.5. (B) Plasmon scattering data fit at Z=0.15 with curves corresponding to T_e=0.1,0.15,0.2. While the relative intensity of the plasmon feature drops with increasing temperature, the spectral position remains constant.

SI. III. COMPARISON WITH REFLECTIVITY MEASUREMENTS

The location of the transition to metal-like behavior has previously been inferred from measurements of optical reflectivity *(S16)*. However, because the optical properties of dense hydrogen are quite complex during transition to the conducting state, it is difficult to infer ionization directly from reflectivity values and make a comparison to the measurements presented in the main text. In order to compare our results with these measurements, we instead used the Born-Mermin dielectric function corresponding to the best fit to the x-ray scattering spectrum and calculated the index of refraction of the plasma at the laser conditions used by Celliers et al. This allowed us to estimate the reflectivity corresponding to the measured x-ray spectrum. In addition, we have compared these results to reflectivities calculated within the Kubo-Greenwood formalism *(S17, S18)* by postprocessing the DFT-MD simulations at the points where XRTS measurements were made. The results are shown in Figure S4, where the continuous line is an optical reflectivity measurement made in compressed D_2 using an 808 nm laser probe, the blue points represent reflectivities inferred from the x-ray scattering fits and the simulations are shown in red. The optical reflectivity and x-ray scattering results appear to be consistent when compared on this basis.

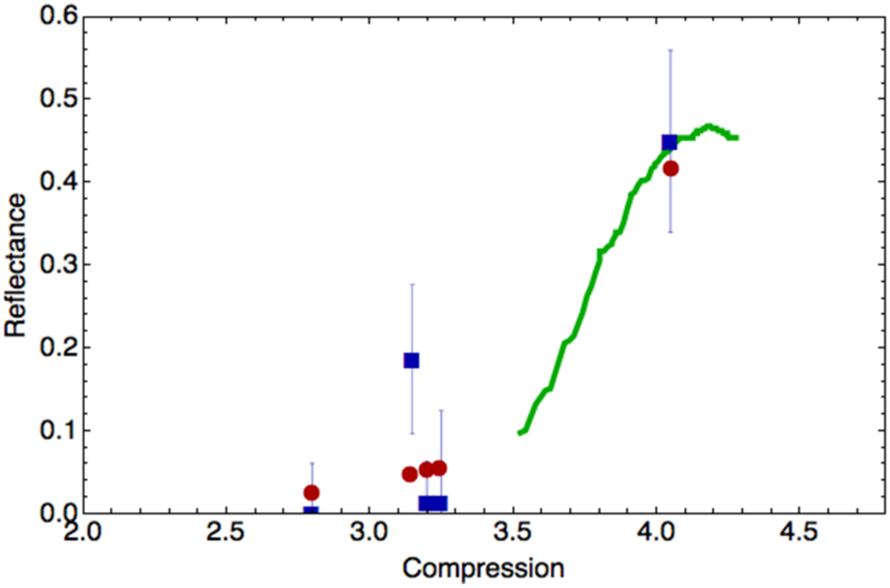

***FIGURE S4:** Previously measured optical reflectivity in compressed D_2 (green) compared with reflectivity inferred from fits to x-ray scattering data (blue). Also shown is optical reflectivity inferred from DFT-MD simulations using the Kubo-Greenwood formalism (red).*

SI. IV. HYDRODYNAMIC SIMULATIONS

Radiation hydrodynamic simulations were performed using the package HYDRA *(S19)*. The simulations are three-temperature (electron, ion and radiative) under the assumption of local thermodynamical equilibrium. The equation of state is similar to QEOS *(S20)*, with a Thomas-Fermi model for ionization and opacities. The laser absorption is modeled with ray tracing, the geometry is one-dimensional with a resolution of 0.25 μm. The equations for the multi-group radiation transport are solved in the diffusive limit, as is the thermal electron conduction, where a flux limiter of 0.05 is used.

We modeled the uncertainty in calculating the final compression by performing simulations for 20% deviations in laser intensity and taking bounding values from the relevant x-ray probe time. Although changes in laser drive conditions can cause significant deviations at early times, the shock decays to a similar set of plasma conditions at x-ray probe time. We note that the calculated shock velocities are consistent with the analytical scaling for laser driven one-dimensional shocks given in *(S21)*.

SI. V. DEUTERIUM EQUATION OF STATE

The deuterium equation of state has generated a great deal of attention and controversy over the last two decades. In particular, the EOS along the primary Hugoniot has been studied extensively, with a focus on the region of maximum compressibility between about 30-200 GPa *(S22)*. The early and widely used Sesame tables *(S23)* predicted a relatively low compressibility (a “stiff” Hugoniot) while some laser experiments suggested a “softer” curve *(S24, S25)*. Updates to the Sesame model *(S26)* and increasingly high resolution ab initio simulations *(S22)* have led to more recent theoretical results between these two extremes.

Experiments at the Omega laser *(S27)* and the Sandia Z-machine *(S28)* have reported smaller differences in the measured Hugoniot. At pressures near 45 GPa, Hicks and coauthors find approximately a 12% difference in compression between the two experimental platforms, after correcting for differences in initial conditions and analysis. The error bars in these measurements are of a similar order, due to the inherent challenges of impedance matching in low density targets. The properties of quartz, typically used as an impedance matching standard in dynamic experiments, have also been shown to play an important role. Re-analysis with an improved quartz standard shifts the high-pressure Omega data toward lower compression and closer agreement with the Z results *(S29)*.

For data analysis and hydrodynamic calculations, we choose the quotidian equation of state (QEOS) *(S20)* that yields compressions between the relatively stiff early Sesame curve *(S23)* and a DFT-MD curve which is softer *(S30)*. At low pressures ~15 GPa where most of our measurements are taken, the variation between these extremes is generally less than 10% – much of the current attention is focused on data above about 30 GPa and compressions greater than 4×. The three curves are plotted in Figure S5 to show the relationship of the QEOS Hugoniot with these bounding curves. The difference between the QEOS Hugoniot and each of these curves is taken as an estimate of EOS-related uncertainty in the compression data plotted in Figure 6 of the main text, where this uncertainty has been added to the error in the VISAR and hydrodynamic calculations. We note that most of our data are taken at compressions of 3.2, where Figure S5 suggests a range of pressure uncertainty from 13-19 GPa.

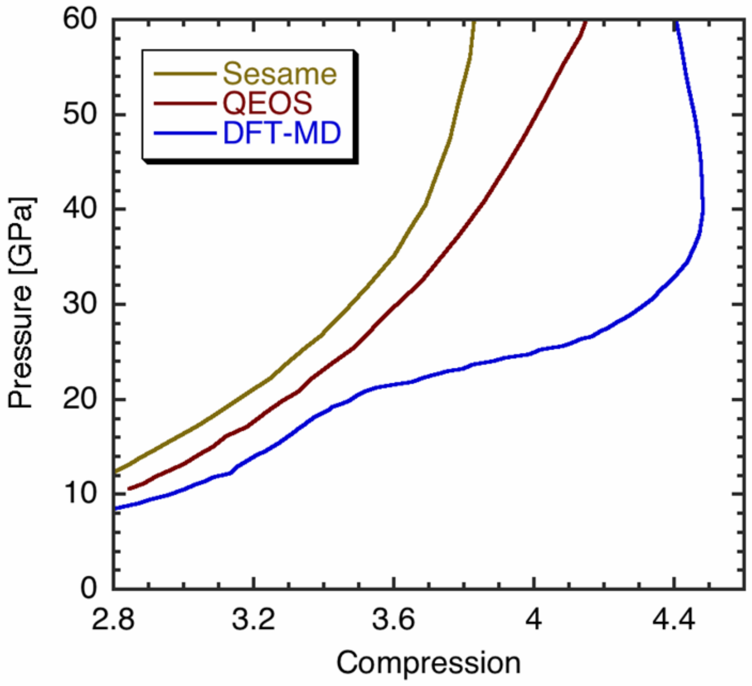

FIGURE S5: The principal Hugoniot of Deuterium (ρ_0=0.17 g/cc) for Sesame *(S23)*, QEOS *(S20)* and the DFT-MD results of Holst et al. *(S31)*.

SI. VI. SIMULATION OF IONIZATION AND DISSOCIATION

We outline the theoretical background of fluid variational theory (FVT) and the framework of density functional theory molecular dynamics (DFT-MD). Both methods were used to estimate the dissociation degree $\alpha = N_D/(N_D+2N_{D2})$, with the number of deuterium atoms N_D and deuterium molecules N_{D2} respectively, along the Hugoniot curve of deuterium, see *(S31)*. The results for α are shown in Fig. 6 of the main text.

The FVT is a free energy minimization scheme for a mixture of hydrogen atoms and molecules, evaluating the chemical reaction $H_2 \Leftrightarrow H + H$ self-consistently (chemical models).

The free energy F of the system is calculated on the basis of the Gibbs-Bogolyubov inequality $F \leq F_0 + \langle \Phi - \Phi_0 \rangle_0$ that states that F is less or equal the sum of the free energies of a reference system F_0 (here a hard sphere system) and the mean value of the difference of two interaction potentials evaluated over the reference states. In our case the reference hard sphere potential Φ_0 and effective two-particle potentials, namely the exponential-6 potentials Φ (see *(S32)* for the molecules and *(S33)* for the atoms) for the real system are used, see *(S34)*.

The equation of state (EOS) and α are direct outputs of the FVT calculation. Since the underlying Hugoniot curve is based on DFT-MD calculations for deuterium, the FVT data have to be mapped to it. Therefore we scaled the density of our FVT hydrogen EOS by a factor of 2, to adjust it to deuterium. We then extracted the FVT EOS points with the respective (FVT)-α according to the EOS points of the underlying DFT-MD Hugoniot curve.

In contrast to FVT, the DFT-MD framework is based on a strictly physical picture. Bound states or other long-living correlations between the electrons and ions are not regarded as new species as in the chemical picture. According to the Born-Oppenheimer approximation the treatment of the ions is classical in the MD and the properties of the electron system are evaluated on the quantum level using the DFT at finite temperatures *(S35)*.

For our simulations we use the VASP program package *(S36-S38)*. To calculate the Coulomb interactions between the electrons and ions more efficiently, projector-augmented wave potentials *(S39, S40)* are used with a converged energy cutoff of 1200 eV.

The forces that act on the ions are derived via the Hellmann-Feynman theorem at each MD step. This procedure is repeatedly performed in a cubic simulation box with periodic boundary conditions for several thousand MD steps of 0.2 fs to 1 fs duration so that the total simulation time amounts up to 8 ps. The ion temperature is controlled with a Nosé thermostat *(S41)*. The most crucial approximation within the DFT is the choice of the exchange-correlation functional for which we use the one of Perdew, Burke, and Ernzerhof (PBE) *(S42)*, a parametrization of the generalized gradient approximation (GGA).

We ensure convergence of our simulation runs with respect to the energy cutoff for the plane wave basis set, the particle number and the **k**-point sets applied for the evaluation of the Brillouin zone. In detail we used 256 atoms and the Baldereschi mean value point *(S43)*.

The dissociation degree for each EOS point along the Hugoniot curve is estimated via the coordination number K(r), a weighted integral over the pair correlation function $g_{ii}(r)$ of the ions, see *(S30)*:

$$K(r) = \frac{N-1}{V} \int_0^r 4\pi r'^2 g_{ii}(r') dr'$$

N is the numer of simulated ions and V the volume of the simulation box. Twice the value of K(r) at the molecule peak, indicated by the dotted line at 0.741Å in Fig. S6, is equal to the number of ions bound to a molecule: $2K(r)=2N_{D2}/(2N_{D2}+N_D)$. Hence the relation between the coordination number and the dissociation degree is $\alpha = 1 - 2K(r)$. Also shown in Fig. S6 are $g_{ii}(r)$ and K(r) for three EOS points along the Hugoniot curve.

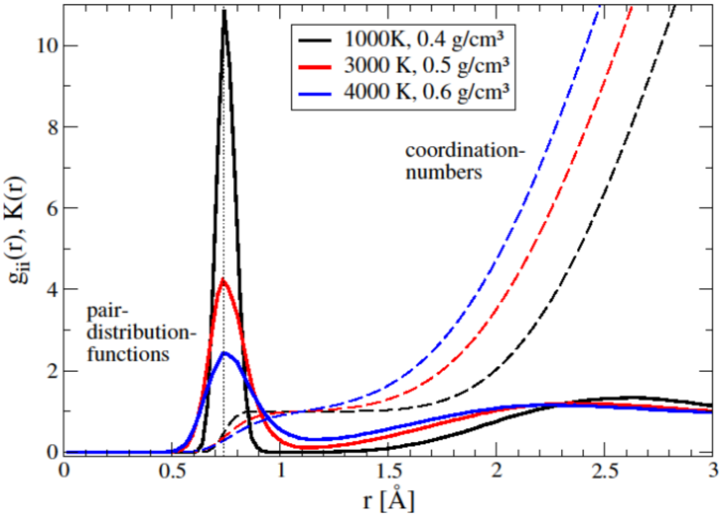

***Figure S6**: Ionic pair distribution functions **g_{ii}(r)** (solid) for several states along the Hugoniot curve together with their corresponding coordination number **K(r)** (dashed). The dotted line indicates the molecular peak at 0.741 Å.*

The simulation box at 1000 K and 0.4 g/cm^3 is shown in Fig. S7(a) with α= 0.0066. As is shown, all ions in the box are bound in molecules. The single ions at the edge are due to the finite box. The respective molecule partner is found in the next box. A box visualizing a much higher dissociation degree of α= 0.427 at 4000 K and 0.6 g/cm^3 is shown in Fig. S7(b). Just about half of the ions are bound to molecules here, leading to a lower molecule peak and a lower coordination number, see Fig. S6.

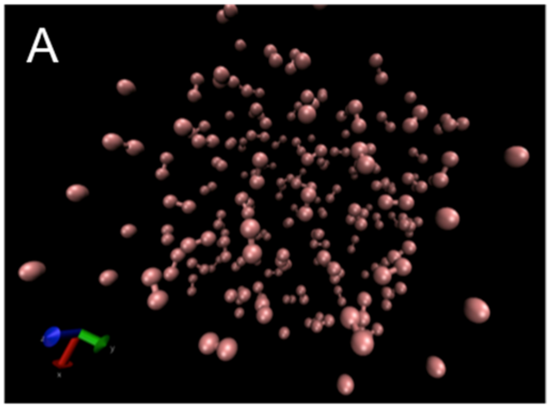

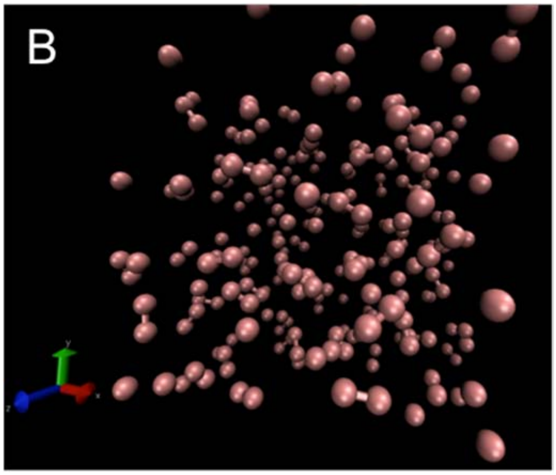

Figure S7. ***(A)*** *View inside the simulation box at 1000 K and 0.4 g/cm^3 with α = 0.0066.* ***(B)*** *View inside the simulation box at 4000 K and 0.6 g/cm^3 with α= 0.427.*

References:

S1. Davis, P., Döppner, T., Glenzer, S. H., Falcone, R. W. & Unites, W. An apparatus for the characterization of warm, dense deuterium. *JINST* **7**, 02004 (2012).

S2. Urry, M. K., Gregori, G., Landen, O.L., Pak, A. & Glenzer, S. H. X-ray probe development for collective scattering measurements in dense plasmas. *J. Quant. Spectr. Rad. Trans.* 99, 636 (2006).

S3. Falk, K. et al. Comparison between x-ray scattering and velocity-interferometry measurements from shocked liquid deuterium. Phys. Rev. E 87, 043112 (2013).

S4. Ichimaru, S. *Basic principles of plasma physics: a statistical approach* (W.A. Benjamin, Reading, MA, 1973).

S5. Redmer, R., Reinholz, H., Röpke, G., Thiele, R. & Höll, A. Theory of X-Ray Thomson Scattering in Dense Plasmas. *IEEE Trans Plasma Sci* 33, 77-84 (2005).

S6. Mermin, N. D., Lindhard dielectric function in the relaxation-time approximation. *Phys. Rev. B* **1**, 2362–2363 (1970)

S7. Thiele, R. *et al.* Plasmon resonance in warm dense matter. *Physical Review E* **78**, 026411 (2008).

S8. Fortmann C., Wierling A. and Röpke G. Influence of local-field corrections on Thomson scattering in collision dominated two-component plasmas. *Phys. Rev. E* **81**, 026405 (2010).

S9. Neumayer, P. et al. Plasmons in Strongly Coupled Shock-Compressed Matter. *Phys. Rev. Lett.* 105, 075003 (2010).

S10. Johnson W. R., Nilsen J. & Cheng K. T. Resonant bound-free contributions to Thomson scattering of X-rays by warm dense matter, *High Energy Density Phys.* **9**, 407 (2013).

S11. Souza A. N., Perkins D. J., Starrett C. E., Saumon D. & Hansen S. B. Predictions of x-ray scattering spectra for warm dense matter. *Phys. Rev. E* **89**, 023108 (2014**).**

S12. Fletcher, L. B. *et al.* Observations of Continuum Depression in Warm Dense Matter with X-Ray Thomson Scattering. *Phys. Rev. Lett.* **112**, 145004 (2014).

S13. Stewart, J. C. and Pyatt Jr., K. D. Lowering of Ionization Potentials in Plasmas *Astrophys. J.* **144**, 1203 (1966).

S14. Ecker, G. and Kröll, W. Lowering of the Ionization Energy for a Plasma in Thermodynamic Equilibrium. *Phys. Fluids* **6**, 62 (1963).

S15. Gericke, D. O., Vorberger, J., Wünsch, K. & Gregori, G. Screening of ionic cores in partially ionized plasmas within linear response. *Phys. Rev. E* **81**, 065401 (2010)

S16. Celliers, P. M. *et al*. Shock-induced transformation of liquid deuterium into a metallic

fluid. *Phys. Rev. Lett.*, **84**, 5564–5567 (2000).

S17. Kubo, R. Statistical-Mechanical Theory of Irreversible Processes. I. General Theory and Simple Applications to Magnetic and Conduction Problems *J. Phys. Soc. Jpn.* **12**, 570 (1957).

S18. Greenwood, D. A. The Boltzmann Equation in the Theory of Electrical Conduction in Metals *Proc. Phys. Soc. London* **71**, 585 (1958).

S19. Marinak, M. M. *et al*. Three-dimensional simulations of Nova high growth factor capsule implosion experiments *Phys. Plasmas* **3**, 2070 (1996).

S20. More, R. M., Warren, K. H., Young, D. A. & Zimmerman, G. B. A new quotidian equation of state (QEOS) for hot dense matter. *Phys. Fluids* **31**, 3059-3078 (1988).

S21. Drake, P. *High-energy-density physics: Fundamentals, Inertial Fusion, and Experimental Astrophysics,* Springer (2006).

S22. McMahon J. M., Morales M. A., Pierleoni C. & Ceperley D. M. The properties of hydrogen and helium under extreme conditions. *Rev Mod Phys.* **84**, 1607–1653 (2012).

S23. Kerley, G. I. Equation of state and phase diagram for dense hydrogen. *Phys. Earth Planet. Inter.* **6**, 78 (1972).

S24.Collins, G. W. *et al*. Measurements of the Equation of State of Deuterium at the Fluid Insulator-Metal Transition. *Science* 281, 1178-1181 (1998).

S25. M. Ross, Linear mixing model for shock-compressed liquid deuterium. *Phys. Rev. B* **58**, 669 (1998).

S26. Kerley, G. I. Sandia National Laboratories Technical Report No. SAND2003-3613 (2003).

S27. Hicks, D. G. *et al*. Laser-driven single shock compression of fluid deuterium from 45 to 220 GPa. *Phys. Rev. B* **79**, 014112 (2009).

S28. Knudson, M. D. et al. Principal Hugoniot, reverberating wave, and mechanical reshock measurements of liquid deuterium to 400 GPa using plate impact techniques. *Phys. Rev. B* 69, 144209 (2004).

S29. Knudson, M. D. & Desjarlais, M. P. Shock Compression of Quartz to 1.6 TPa: Redefining a Pressure Standard *Phys. Rev. Lett.* **103**, 225501 (2009).

S30. Holst, B., Redmer, R. & Desjarlais, M. P. Thermophysical properties of warm, dense hydrogen using quantum molecular dynamics simulations. *Phys. Rev. B* **77**, 184201 (2008).

S31. Holst, B., Redmer, R., Gryaznov, V., Fortov, V. & Iosilevskiy, I. Hydrogen and deuterium in shock wave experiments, ab initio simulations and chemical picture modeling *Eur. Phys. J. D* **66**, 104 (2012).

S32. Ross, M., Ree, F. H. & Young, D. A. The equation of state of molecular hydrogen at very high density *J. Chem. Phys.* **79**, 1487 (1983).

S33. Ree, F. H. in *Shock Waves in Condensed Matter* 1987, edited by S. Schmidt and N. Holmes (Elesevier, New York, 1988) pp. 125–130.

S34. Juranek, H., Redmer, R. & Rosenfeld, Y. Fluid variational theory for pressure dissociation in dense hydrogen: Multicomponent reference system and nonadditivity effects *J. Chem. Phys*. **117**, 1768 (2002).

S35. Mermin, N. D. Thermal Properties of the Inhomogeneous Electron Gas *Phys. Rev.* **137**, A1441 (1965).

S36. Kresse, G. & Hafner, J. *Ab initio* molecular dynamics for liquid metals *Phys. Rev. B* **47**, 558 (1993).

S37. Kresse, G. & Hafner, J. *Ab initio* molecular-dynamics simulation of the liquid-metal–amorphous-semiconductor transition in germanium *Phys. Rev. B* **49**, 14251 (1994).

S38. Kresse, G. & Furthmüller, J. Efficient iterative schemes for *ab initio* total-energy calculations using a plane-wave basis set *Phys. Rev. B* **54**, 11169 (1996).

S39. Blöchl, P. E. Projector augmented-wave method *Phys. Rev. B* **50**, 17953 (1994).

S40. Kresse, G. & Joubert, D. From ultrasoft pseudopotentials to the projector augmented-wave method *Phys. Rev. B* **59**, 1758 (1999).

S41. Nosé, S. A unified formulation of the constant temperature molecular dynamics methods *J. Chem. Phys*. **81**, 511 (1984).

S42. Perdew, J. P., Burke, K. & Ernzerhof, M. Generalized gradient approximation made simple *Phys. Rev. Lett*. **77**, 3865 (1996).

S43. Baldereschi, A. Mean-value point in the Brillouin zone *Phys. Rev. B* **7**, 5212 (1973).